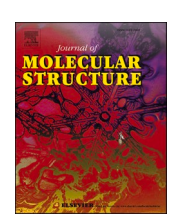
ELSEVIER

Contents lists available at ScienceDirect

#### Journal of Molecular Structure

journal homepage: www.elsevier.com/locate/molstr





## Synthesis of thiophene-appended pyrazolines via citrus juice-assisted cyclocondensation: Characterization, crystal studies, computational analysis, and anti-angiogenic potential

Chandan Mallikarjuna <sup>a</sup>, Udaya Kumar A H <sup>b,c</sup>, Mahesha <sup>b,d</sup>, Rekha N Dharmappa <sup>e</sup>, Deepashree Nagaraj <sup>a</sup>, Neratur Krishnappagowda Lokanath <sup>b</sup>, Kariyappa Ajay Kumar <sup>a,\*</sup>

- <sup>a</sup> Department of Chemistry, Yuvaraja College, University of Mysore, Mysuru, 570005 Karnataka, India
- <sup>b</sup> Department of Studies in Physics, University of Mysore, Manasagangotri, Mysuru 570006 Karnataka, India
- <sup>c</sup> Department of Physics, Seshadripuram Institute of Technology, Mysuru, 571311 Karnataka, India
- <sup>d</sup> Department of Physics, SJCE, JSS Science and Technology University, Mysuru 570006 Karnataka, India
- e Postgraduate Department of Biotechnology, JSS College of Arts, Commerce, Ooty Road, Mysuru 570 025 Karnataka, India

#### ARTICLE INFO

# Keywords: Pyrazolines;Thiophene Green synthesis X-ray diffraction DFT calculations C-MET receptor

#### ABSTRACT

A series of thiophene-tethered pyrazoline derivatives (5a-h) were synthesized via a green cyclocondensation reaction between chalcones and substituted phenylhydrazines, utilizing citrus fruit extract as an environmentally benign reaction medium. The compounds were obtained in yields ranging from 72 to 89 %. Structural characterization was performed using <sup>1</sup>H and <sup>13</sup>C NMR spectroscopy and mass spectrometry, while compound **5** g was further characterized by single-crystal X-ray diffraction, revealing an envelope conformation with distinct dihedral angles of  $6.78^{\circ}$ ,  $10.77^{\circ}$ , and  $88.6^{\circ}$  between the pyrazoline and attached aromatic rings. Hirshfeld surface analysis revealed dominant H···H and C···H interactions in the crystal packing, while energy framework analysis indicated that dispersion energy (-249.8 kJ/mol) was the most significant stabilizing factor. Density Functional Theory (DFT) calculations (APFD/6-311++G(d,p)) showed that compound **5h** exhibited the lowest HOMO-LUMO gap (3.17 eV), highest electron affinity (1.82 eV), and lowest ionization potential (4.99 eV), suggesting high reactivity, while compound 5f was the most electronically stable. Electrostatic potential maps of 5 g and 5 h indicated regions of strong nucleophilic and electrophilic potential. Anti-angiogenic activity was evaluated using the chorioallantoic membrane (CAM) assay, where compounds 5a, 5c, 5 g, and 5 h significantly reduced microvessel density compared to control groups. Molecular docking studies against the c-Met tyrosine kinase receptor revealed strong binding affinities, with docking scores ranging from -6.7 to -9.1 kcal/mol. Compound 5c, with the highest theoretical pKd value of 6.68, demonstrated the strongest binding affinity, while compound 5a formed a key hydrogen bond with ASP1046, with the centroid of its pyrazoline ring positioned 2.78 Å from the receptor, indicating a stable interaction. These findings highlight the potential of thiophenelinked pyrazolines as promising candidates for anti-angiogenic drug development.

#### 1. Introduction

The World Health Organization's most recent global cancer statistics indicate a substantial rise in cancer cases, reaching 19.3 million new diagnoses annually, with cancer now responsible for around 15 % of all deaths globally. This alarming trend underscores the urgent need for more effective and selective cancer therapies. While targeted chemotherapy remains a central approach in oncology, its success is often limited by poor selectivity and the emergence of drug resistance. As a

result, there is a growing demand for novel anticancer agents that are both potent and exhibit reduced systemic toxicity [1]. Among emerging strategies in cancer therapy, angiogenesis inhibition has gained prominence due to its ability to starve tumors of the blood supply essential for growth and metastasis [2]. Angiogenesis refers to the formation of new blood vessels from pre-existing ones and is a tightly regulated process controlled by a complex interplay of both pro- and anti-angiogenic factors. This balance ensures proper microvessel growth under physiological conditions. However, in cancer, this regulation is disrupted.

E-mail address: ajaykumar@ycm.uni-mysore.ac.in (K.A. Kumar).

https://doi.org/10.1016/j.molstruc.2025.142959

<sup>\*</sup> Corresponding author.

Understanding how tumors, at specific stages, drive the establishment and proliferation of new microvessels remains one of the most challenging aspects of cancer research. Since prolonged tumor growth depends on sustained angiogenesis, this dependency has prompted the development of alternative cancer therapies that specifically target the growth of tumor-associated microvessels [3]. Targeting angiogenic pathways such as VEGF/VEGFR and c-Met/HGF effectively disrupts angiogenesis and impedes tumor growth [4]. The c-Met receptor, also known as mesenchymal-epithelial transition factor, is a tyrosine kinase activated by hepatocyte growth factor (HGF). Upon HGF binding, c-Met undergoes dimerization and activates downstream signaling pathways involved in cell growth, migration, angiogenesis, and invasion. Dysregulation of the c-Met/HGF signaling axis, often due to mutations or abnormal expression, is frequently observed in various cancers and is closely linked to tumor development and progression. This makes c-Met a high value target for anti-angiogenic drug development [5]. Small-molecule inhibitors that disrupt angiogenic pathways offer a promising alternative to traditional chemotherapy, with the potential to overcome resistance mechanisms while minimizing off-target toxicity [3]. In this context, azaheterocyclic scaffolds such as pyrazoles, isoxazoles, and their hybrid derivatives have emerged as promising angiostatic agents due to their favorable biological profiles; however, there remains a critical need to identify novel structures that offer both high potency and selectivity [6,7]. Recent studies have particularly highlighted the anticancer potential of hybrid heterocyclic compounds, such as pyrazolines, due to their significant cytotoxic effects against various cancer cell lines [8]. Among these, thiophene-tethered pyrazoline derivatives have garnered significant attention in medicinal chemistry due to their diverse pharmacological activities and structural versatility. The thiophene ring imparts aromatic stability and electron-rich characteristics, facilitating interactions with biological targets [9], while pyrazole rings are recognized bioactive scaffolds with anti-inflammatory, antimicrobial, and anticancer properties [10]. The fusion of these two motifs enhances the overall biological profile of the compounds, offering a synergistic effect that can lead to improved efficacy and selectivity. Importantly, several thiophene-pyrazoline hybrids have demonstrated cytotoxic effects in human cancer cell lines, positioning them as promising lead compounds in anticancer drug development [11]. The skeleton is an abundant resource of biologically significant molecules with a wide range of biological and pharmacological properties including anti-inflammatory [12], anti-diabetic [13], anti-cancer properties [14,15]. The investigation of condensed heterocyclic scaffolds plays a pivotal role in expanding the chemical space of bioactive compounds while also offering theoretical insights into structure-reactivity relationships and fostering the development of novel synthetic methodologies [16]. The pharmacological relevance of this scaffold is underscored by its presence in several clinically approved drugs, such as the tyrosine kinase inhibitor (TKI) crizotinib [17], the beta-lactam antibiotic and antibacterial cefoselis [18], the antidepressant drug dorzolamide [19], the analgesic difenamizole [20], the anti-inflammatory drug ramifenazone [21], the diuretic muzolimine [22], the antipsychotic agent 3-cyano-N-(1,3-diphenyl-1H-pyrazol-5-yl) benzamide (CDPPB) [23] and the H2-receptor agonist betazole [24]. In recent findings, compound (A) emerged as a potent and selective c-Met inhibitor (IC50  $= 5.17 \pm 0.48$  nM), showing efficacy comparable to the standard drug cabozantinib [25]. Compound (B) exhibited potent selective inhibition of EGFR and VEGFR-2, showing significant anti-proliferative effects on NSCLC cells, particularly A549 and H441, and were more effective against EGFR-mutated cell lines than gefitinib, while also inducing G2/M cell cycle arrest, promoting apoptosis, and inhibiting cell migration [26]. Compound (C) demonstrated strong dual inhibition of VEGFR2 and CDK-2, with IC50 values of 0.2  $\mu M$  (93.2 %inhibition) for VEGFR2 and 0.458 µM (88.7 % inhibition) for CDK-2 [27]. Furthermore, compound (D) showed selective cytotoxicity against MCF-7 breast cancer cells (IC50 =  $7.31 \mu M$ ), linked to mitochondrial damage and caspase-mediated apoptosis, reinforcing the

therapeutic promise of pyrazoline-based hybrids [28] (Fig. 1). In modern drug discovery, computational approaches such as molecular docking and quantum chemical calculations via Density Functional Theory (DFT) are indispensable tools. Docking studies enable prediction of ligand-protein interactions and binding affinities, which help prioritize candidates for synthesis and biological evaluation. For example, several studies have reported effective docking of pyrazole-based and hydrazone derivatives against biological targets involved in cancer and viral replication, validating their therapeutic potential [29-31]. Quantum chemical calculations using Density Functional Theory (DFT) have become indispensable in modern drug discovery for modeling molecular properties and predicting biological reactivity. DFT enables the identification of active sites in drug molecules and facilitates the correlation of electronic structure with observed pharmacological effects. By analyzing frontier molecular orbitals (FMOs) including HOMO-LUMO energies, energy gap, electrophilicity, and softness indices-DFT provides valuable insights into charge transfer behavior, local reactivity, and bioactivity potential of small molecules, thus aiding in the rational design of more effective therapeutic agents [32–34].

In light of these considerations, this study explores the synthesis of a series of thiophene-linked pyrazoline derivatives and investigates their structural, computational, and biological characteristics with a focus on anti-angiogenic activity. Through a combination of green chemistry approaches, spectroscopic and crystallographic characterization, and *invivo* CAM assay analysis, the study aims to contribute novel insights into the development of targeted small-molecule inhibitors with potential applications in cancer therapy.

#### 2. Experimental

#### 2.1. Materials and methods

All chemicals were obtained from Sigma Aldrich and were used as received without additional purification. Thin layer chromatography (TLC) utilizing hexane: ethyl acetate (4:1) as the solvent system was used to monitor the reaction on precoated silica gel plates.  $^1\mathrm{H}$  NMR (400 MHz) and  $^{13}\mathrm{C}$  NMR (101 MHz) spectra were obtained on an Agilent NMR spectrometer. TMS served as the internal standard, while CDCl3 was used as the solvent, and chemical shifts were reported in ppm. Mass spectra were obtained on the Lynx SCN781 spectrometer (TOF mode) using electrospray ionization (ESI $^+$ ). Melting temperatures were determined using the open capillary technique.

#### 2.2. General procedure for the synthesis of chalcone (3)

The intermediate chalcone compound is synthesized via a Claisen-Schmidt condensation reaction using the appropriate aldehydes and ketones. Specifically, 2-formylthiophene (3.27 mL, 0.035 mol) and acetone (1.2 mL, 0.017 mol) were dissolved in methanol (10 mL) and mixed for about 10 min to achieve a uniform solution. A solution of NaOH (2.12 g, 0.053 mol) in a small amount of water was gradually added to this mixture over 30 min. After six hours of stirring at 10  $^{\circ}$ C, the reaction mixture, which had started out light brown, turned yellow. Thin layer chromatography was used to track the reaction's progress. After the reaction was complete, the mixture was poured into crushed ice and left to stand overnight to allow the precipitate to form. The precipitate was then filtered, dried and further purified by silica gel column chromatography using hexane/ethyl acetate (4:1) as the mobile phase to obtain the pure product.

#### 2.2.1. Synthesis of thienyl-pyrazolines, 5(a-h)

The desired pyrazoline compounds were synthesized through a cyclocondensation reaction involving the appropriate chalcone (3) and phenylhydrazine hydrochloride (4a-h) in the presence of citrus fruit juice and tetrabutylammonium bromide (TBAB) in methanol [35]. The citrus juice is obtained by squeezing the pulp of the lemon species, Kagzi

Fig. 1. Various marketed drugs and kinase inhibitors (A,B, C and D) containing pyrazoline-motifs.

lime (*Citrus aurantiifolia*), diluting it with water, stirring, heating at  $45-50\,^{\circ}$ C for 30 min, and filtering to yield a smooth juice. The juice typically contains citric acid (4–6 %), ascorbic acid (44.6 mg/100 mL), flavonoids (70.6 mg/100 mL), and other bioactive compounds, providing a mildly acidic medium (pH ~2.5–3.0) for the reaction [36]. A chalcone compound (0.98 g, 0.004 mol) and phenylhydrazine hydrochloride (0.008 mol) were dissolved in methanol (10 mL), and freshly prepared lemon juice (10 mL) was added, followed by the addition of tetrabutylammonium bromide (TBAB) (0.12 g, 0.0004 mol). The mixture was then stirred under reflux conditions for 4 h. After the reaction, the mixture was quenched with ice water and allowed to stand overnight to form a precipitate. The resulting product was filtered and dried. The pyrazoline compounds were purified by silica gel column chromatography using hexane/ethyl acetate (4:1) as the mobile phase to get pure compounds 5(a-h) in excellent yield.

#### Analytical data of compounds, 5(a-h)

## (E)-1-Phenyl-5-(thiophen-2-yl)-3-(2-(thiophen-2-yl)vinyl)-4,5-dihydro-1H-pyrazole (5a)

Canary yellow solid; Yield:84 %; mp:138–140 °C;  $^{1}$ H NMR (400 MHz, CDCl<sub>3</sub>)  $\delta$  7.27 (d, J = 5.1 Hz, 1H), 7.23 (dd, J = 5.0, 1.3 Hz, 1H), 7.17 (d, J = 2.2 Hz, 1H), 7.16 (d, J = 2.2 Hz, 1H), 7.07 (d, J = 3.5 Hz, 1H), 7.01(d, J = 6.2 Hz, 1H), 7.04 (t, J = 2.7 Hz, 2H), 7.02 (dd, J = 3.3, 1.6 Hz, 2H), 6.98 (dd, J = 3.5, 0.7 Hz, 1H), 6.95 (dd, J = 5.0, 3.5 Hz, 1H), 6.76 (d, J = 16.0 Hz, 1H), 5.51 (dd, J = 11.8, 6.3 Hz, 1H), 3.67 (dd, J = 16.7, 11.9 Hz, 1H), 3.15 (dd, J = 16.7, 6.3 Hz, 1H).  $^{13}$ C NMR (101 MHz, CDCl<sub>3</sub>)  $\delta$  148.86, 145.06, 142.74, 142.02, 128.86, 127.86, 127.07, 126.95, 126.32, 125.73, 125.14, 124.64, 124.41, 120.78, 114.94, 60.15, 42.56. MS (ESI $^+$ ) m/z: Calcd: (M+1) 337.47, found: (M+1) 337.44

## (E)-1-(2-Chlorophenyl)-5-(thiophen-2-yl)-3-(2-(thiophen-2-yl) vinyl)-4,5-dihydro-1H-pyrazole (5b)

Greenish yellow solid; Yield:72 %; mp:144–146 °C;  $^1\mathrm{H}$  NMR (400 MHz, CDCl3):  $\delta$  7.31 (dd,  $J=8.1,\,1.6$  Hz, 1H), 7.27 (d, J=1.4 Hz, 1H), 7.25 (d, J=1.5 Hz, 1H), 7.12 – 7.00 (m,5H), 6.94 – 6.85 (m,2H), 6.80 (dd,  $J=3.5,\,1.1$  Hz,1H), 6.72 (dd,  $J=5.1,\,3.5$  Hz,1H), 6.14 (dd, J=

10.7, 6.2 Hz,1H), 3.58 (dd, J=16.4, 10.7 Hz, 1H), 3.34 (dd, J=16.4, 6.0 Hz, 1H).  $^{13}$ C NMR (101 MHz, CDCl<sub>3</sub>):  $\delta$  151.32, 142.33, 142.20, 129.97, 127.96, 127.18, 127.12, 126.59, 126.35, 125.03, 125.84, 125.00, 124.94, 124.46, 121.24, 77.47, 77.36, 77.16, 76.84, 61.84, 40.84. MS (ESI<sup>+</sup>) m/z: Calcd: (M+1) 371.91, found: (M+1) 371.42

## (E)-1-(3-Chlorophenyl)-5-(thiophen-2-yl)-3-(2-(thiophen-2-yl) vinyl)-4,5-dihydro-1H-pyrazole (5c)

Greenish yellow solid; Yield :82 %; mp:140–142 °C;  $^{1}$ H NMR (400 MHz, CDCl<sub>3</sub>)  $\delta$  7.29 – 7.26 (m, 1H), 7.25 – 7.21 (m, 2H), 7.14 – 7.07 (m, 2H), 7.05 – 6.99 (m, 3H), 6.96 (dd, J = 5.0, 3.5 Hz, 1H), 6.89 (dd, J = 2.2, 0.8 Hz, 1H), 6.84 – 6.77 (m, 2H), 5.50 (dd, J = 11.8, 6.0 Hz, 1H), 3.65 (dd, J = 16.7, 11.8 Hz, 1H), 3.14 (dd, J = 16.7, 6.0 Hz, 1H).  $^{13}$ C NMR (101 MHz, CDCl<sub>3</sub>)  $\delta$  149.17, 145.13, 144.99, 141.97, 134.84, 129.94, 127.90, 127.13, 127.10, 126.62, 125.84, 125.18, 124.44, 120.71, 119.57, 113.92, 111.62, 59.90, 42.54. MS (ESI $^{+}$ ) m/z: Calcd: (M + 1) 371.91, found: (M + 1) 371.44.

## (E)-1-(4-Chlorophenyl)-5-(thiophen-2-yl)-3-(2-(thiophen-2-yl) vinyl)-4,5-dihydro-1H-pyrazole (5d)

Lemon yellow solid; Yield :76 %; mp:130–132 °C;  $^{1}$ H NMR (400 MHz, CDCl<sub>3</sub>)  $\delta$  7.27 (d, J = 5.1 Hz, 1H), 7.23 (dd, J = 5.0, 1.3 Hz, 1H), 7.17 (d, J = 2.2 Hz, 1H), 7.16 (d, J = 2.2 Hz, 1H), 7.07 (d, J = 3.5 Hz, 1H), 7.04 (t, J = 2.7 Hz, 2H), 7.02 (dd, J = 3.3, 1.6 Hz, 2H), 6.98 (dd, J = 3.5, 0.7 Hz, 1H), 6.95 (dd, J = 5.0, 3.5 Hz, 1H), 6.76 (d, J = 16.0 Hz, 1H), 5.51 (dd, J = 11.8, 6.3 Hz, 1H), 3.67 (dd, J = 16.7, 11.9 Hz, 1H), 3.15 (dd, J = 16.7, 6.3 Hz, 1H).  $^{13}$ C NMR (101 MHz, CDCl<sub>3</sub>)  $\delta$  148.86, 145.06, 142.74, 142.02, 128.86, 127.86, 127.07, 126.95, 126.32, 125.73, 125.14, 124.64, 124.41, 120.78, 114.94, 60.15, 42.56. MS (ESI $^+$ ) m/z: Calcd: (M + 1) 370.91, found: (M + 1) 371.42.

## (E)-1-(4-Fluorophenyl)-5-(thiophen-2-yl)-3-(2-(thiophen-2-yl) vinyl)-4,5-dihydro-1H-pyrazole (5e)

Brownish yellow solid; Yield :86 %; mp:128–130 °C;  $^1$ H NMR (400 MHz,)  $\delta$  7.36 (d, J=6.3 Hz, 1H), 7.24 – 7.18 (m, 2H), 7.15 – 7.11 (m, 2H), 7.04 (d, J=3.3 Hz, 1H), 7.01 – 6.98 (m, 3H), 6.95 (dd, J=3.3, 1.4 Hz, 1H), 6.91 (dd, J=5.0, 3.5 Hz, 1H), 6.71 (d, J=3.1 Hz, 1H), 5.47

(dd, J = 11.8, 6.3 Hz, 1H), 3.63 (dd, J = 16.7, 11.8 Hz, 1H), 3.11 (dd, J = 16.7, 6.3 Hz, 1H).  $^{13}$ C NMR (101 MHz, CDCl<sub>3</sub>)  $\delta$  148.94, 145.13, 142.82, 142.08, 128.93, 127.92, 127.13, 127.02, 126.40, 125.79, 125.20, 124.73, 124.48, 120.84, 115.03, 60.23, 42.63. MS (ESI<sup>+</sup>) m/z: Calcd: (M + 1) 355.06, found: (M + 1) 355.13.

## (E)-1-(4-Bromophenyl)-5-(thiophen-2-yl)-3-(2-(thiophen-2-yl) vinyl)-4,5-dihydro-1H-pyrazole (5f)

Greenish yellow solid; Yield :80 %; mp:142–144 °C;  $^1$ H NMR (400 MHz, CDCl<sub>3</sub>)  $\delta$  7.29 (d, J=2.1 Hz,1H), 7.27 (s,1H), 7.25 (d, J=5.1 Hz,1H), 7.21 (dd, J=5.0, 1.3 Hz,1H), 7.06 (d, J=3.5 Hz,1H), 7.03 – 6.91 (m,6H), 6.74 (d, J=16.1 Hz,1H), 5.49 (dd, J=11.8, 6.2 Hz,1H), 3.65 (dd, J=16.8, 11.9 Hz,1H), 3.13 (dd, J=16.7, 6.2 Hz, 1H).  $^{13}$ C NMR (101 MHz, CDCl<sub>3</sub>)  $\delta$  149.03, 145.11, 143.24, 142.13, 131.86, 127.97, 127.19, 127.07, 126.49, 125.86, 125.26, 124.53, 120.89, 115.49, 112.10, 77.47, 77.16, 76.84, 60.15, 42.68. MS (ESI $^+$ ) m/z: Calcd: (M+1) 415.37, found: (M+1) 415.41.

## (E)-4-(5-(Thiophen-2-yl)-3-(2-(thiophen-2-yl)vinyl)-4,5-dihydro-1H-pyrazol-1-yl)benzonitrile (5 g)

Light yellow solid; Yield :83 %; mp:136–138 °C;  $^1$ H NMR (400 MHz, CDCl<sub>3</sub>)  $\delta$  7.56 – 7.52 (m,3H), 7.36 (dd, J = 5.0, 1.2 Hz,1H), 7.26 (d, J = 3.5 Hz,1H), 7.11 – 7.04 (m,5H), 6.91 (dd, J = 5.0, 3.5 Hz,2H), 5.95 (dd, J = 11.5, Hz,1H), 3.70 (dd, J = 16.8, 11.5 Hz,1H), 3.13 (dd, J = 16.9, 6.2 Hz,1H).  $^{13}$ C NMR (101 MHz, CDCl<sub>3</sub>)  $\delta$  157.86, 155.06, 142.94, 142.32, 128.76, 127.56, 127.04, 126.95, 126.42, 125.93, 125.44, 124.84, 124.31, 120.98, 114.94, 60.55, 42.36.

## (E)-1-(4-Methoxyphenyl)-5-(thiophen-2-yl)-3-(20-(thiophen-2-yl) vinyl)-4,5-dihydro-1H-pyrazole (5h)

Golden yellow solid; Yield :77 %; mp:122–124 °C;  $^1\mathrm{H}$  NMR (400 MHz, CDCl<sub>3</sub>)  $\delta$  7.24 – 7.18 (m, 2H), 7.06 – 7.02 (m, 3H), 7.01 – 6.96 (m, 3H), 6.95 – 6.91 (m, 1H), 6.81 – 6.76 (m, 2H), 6.70 (d, J=16.1 Hz, 1H), 5.41 (dd, J=11.7, 7.4 Hz, 1H), 3.74 (s, 3H), 3.61 (dd, J=16.5, 11.7 Hz, 1H), 3.09 (dd, J=16.5, 7.4 Hz, 1H).  $^{13}\mathrm{C}$  NMR (101 MHz, CDCl<sub>3</sub>)  $\delta$  153.88, 148.06, 145.76, 142.30, 138.86, 127.81, 126.97, 126.57, 125.37, 125.00, 124.43, 121.19, 115.63, 114.40, 61.42, 55.57, 42.54. MS (ESI $^+$ ) m/z: Calcd: (M + 1) 367.50, found: (M + 1) 367.48.

#### 2.2.2. Specrtal characterization of 5a-5h

The  $^1H$  NMR spectra of the synthesized pyrazoline derivatives (5a–5h) display distinct and characteristic splitting patterns that confirm the successful formation of the pyrazoline ring. Three pyrazoline hydrogens resonate in the region  $\delta$  3.09–3.34 ppm ( $H_a$ ),  $\delta$  3.58–3.70 ppm ( $H_b$ ), and  $\delta$  5.41–6.14 ppm ( $H_x$ ). These protons appeared as doublets of doublets due to coupling between three magnetically nonequivalent hydrogens, as shown in a typical ABX representation (Fig. 2). The two diastereotopic methylene protons ( $H_a$  and  $H_b$ ) consistently appear in the lower field regions, exhibiting geminal coupling constants in the range of 16.4–16.9 Hz, which are characteristic of nonequivalent methylene protons adjacent to a nitrogen atom. Additionally, these methylene protons show vicinal coupling with the neighboring methine proton ( $H_x$ ) in the range of 3.9–11.9 Hz, depending on the

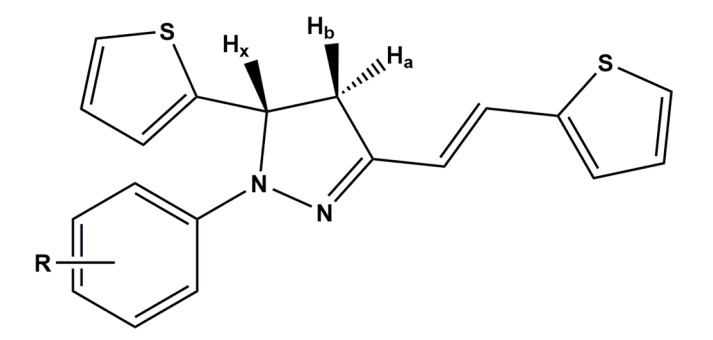


Fig. 2. ABX-Type Representation of Protons  $(H_a,\ H_b,\ H_x)$  in Pyrazoline Compounds.

substitution pattern. The methine proton appears in the mid-field region confirming its position within the five-membered pyrazoline ring. The vinylic proton, located adjacent to the pyrazoline ring, is observed as a doublet at  $\delta$  6.70–6.76 ppm with a large coupling constant (~16 Hz), characteristic of a trans-olefinic configuration. These coupling patterns and chemical shifts are in excellent agreement with the expected ring geometry and substitution, confirming successful cyclization. In the aromatic region (δ 6.92–7.56 ppm), multiplets correspond to protons on the phenyl and thiophene moieties. The splitting patterns and integration values reflect the substitution patterns on the aromatic rings. Electron-donating groups (e.g., methoxy) cause slight upfield shifts due to increased electron density, whereas electron-withdrawing groups (e. g., fluoro, cyano, bromo) lead to downfield shifts due to deshielding effects. In the <sup>13</sup>C NMR spectra, the methylene and methine carbons within the pyrazoline ring are clearly observed at approximately  $\delta$  42 ppm and  $\delta$  60 ppm, respectively. Signals in the  $\delta$  112.8–157.8 ppm range are attributed to aromatic and alkenyl carbons, with chemical shift variations influenced by the electronic nature of ring substituents. Notably, compound 5 g exhibits a diagnostic carbon signal at  $\delta$  157.86 ppm attributable to the nitrile carbon, while **5h** shows a resonance at  $\delta$ 55.57 ppm for the methoxy group. Additionally, the mass spectra of all compounds (5a-5h) show molecular ion peaks ([M]\*) consistent with their calculated molecular weights, further confirming the proposed structures.

#### 2.3. Angioinhibitory effect by chorioallantoic membrane (CAM) assay

The chorioallantoic membrane (CAM) assay is a widely accepted in vivo model for evaluating the anti-angiogenic potential of bioactive compounds due to its high vascularity, ease of manipulation, and costeffectiveness. In this study, the CAM assay was employed to assess the angiogenesis-inhibitory activity of the synthesized pyrazoline derivatives (5a-h), following the procedure described by Rekha et al. [37]. Fertilized hen eggs were surface-sterilized with 70 % ethanol and incubated in a humidified, fan-assisted incubator at 37  $^{\circ}\text{C}$  to facilitate embryonic development. On day 8 of incubation, a small window was created on the eggshell to expose the CAM, and Whatman paper discs (2 mm in diameter) impregnated with 100 µg of each test compound were gently placed over regions with prominent blood vessel branching. The windows were resealed with sterile cellophane tape, and the eggs were incubated for an additional 24 h. Following incubation, the CAMs were visually examined for any reduction or regression in vascularization around the treated area. A significant reduction in microvessel density, as compared to untreated controls, was interpreted as positive antiangiogenic activity.

#### 2.4. Single crystal structural analysis

A high-quality, well-grown single crystal was selected using an Olympus polarizing microscope for single-crystal X-ray diffraction analysis. The XtaLAB Pro II AFC12 (RINC) Kappa single-crystal diffractometer with graphite-monochromated Mo-Ka radiation at a wavelength of 0.711 Å was used for data collection. Complete data were collected through omega ( $\omega$ ) scans at a step size of 0.7° per frame, with an acquisition time of 11.0 s per scan. The diffraction patterns were indexed, and an optimized data collection plan was generated using the CrysAlisPro software (Rigaku, version 1.171.41.123a, 2022). Data reduction, scaling, and absorption corrections were also performed with CrysAlisPro [38]. The crystal structure was solved using SHELXT, followed by refinement with the least squares method in SHELXL version 2018/3 within the Olex-2 software [39-41]. Anisotropic displacement parameters were assigned to all non-hydrogen atoms, while hydrogen atoms were refined isotropically with a riding model based on established bonding geometries. Geometric parameters, including bond lengths, angles, and torsional angles, were analyzed using the Platon software and are provided in Table 1 [42]. The Mercury software

**Table 1**The crystallographic table along with CCDC number of compound 5 g.

CCDC No	2410,391
Empirical formula	$C_{20}H_{15}N_3S_2$
Formula weight	361.47
Temperature/K	293(2)
Crystal system	Monoclinic
Space group	P2 <sub>1</sub> /n
a/Å	8.2877(2)
b/Å	11.1323(4)
c/Å	19.7785(6)
$\alpha/^{\circ}$	90
β/°	97.350(3)
γ/°	90
Volume/Å <sup>3</sup>	1809.79(10)
Z	4
$\rho_{calc} g/cm^3$	1.327
μ/mm <sup>-1</sup>	0.301
F(000)	752.0
Radiation	MoKα ( $\lambda = 0.71073$ )
2Θ range for data collection/°	4.152 to 56.278
Index ranges	$-10 \le h \le 10$ , $-14 \le k \le 8$ , $-25 \le l \le 25$
Reflections collected	20,119
Independent reflections	4245 [ $R_{int}$ =0.0260, $R_{sigma}$ = 0.0252]
Data/restraints/parameters	4245/160/309
Goodness-of-fit on F <sup>2</sup>	1.042
Final R indexes $[I>=2\sigma(I)]$	$R_1 = 0.0380, wR_2 = 0.0950$
Final R indexes [all data]	$R_1 = 0.0576$ , $wR_2 = 0.1050$
Largest diff. peak/hole / e $\mathring{A}^{-3}$	0.18/-0.21

package was used for visualizing the crystal structure and creating crystal packing diagrams to illustrate intermolecular interactions [43].

#### 3. Computational details

#### 3.1. Hirsfeld surface analysis

Hirshfeld surface analysis has emerged as a key qualitative method for studying intermolecular interactions in crystal structures. The *Crystal Explorer* software is used for visualizing molecular crystal structures, particularly through its 3D Hirshfeld surfaces and associated 2D fingerprint plots. These surfaces are derived from the total electron density of a molecule and its neighbouring environment, offering insights into crystal packing and intermolecular interactions. The normalized contact distance ( $d_{norm}$ ), is a critical parameter for analyzing interactions. A colour scheme highlights interaction strength: red for strong, white for weak, and blue for no interaction. Additional 3D surface features like shape index and curvedness aid in identifying interactions such as  $C-H...\pi$  and  $\pi...\pi$  stacking. Two-dimensional fingerprint plots provide a quantitative representation of molecular interactions, with spikes indicating significant contributions to crystal packing [44,45].

#### 3.2. DFT studies

Density Functional Theory (DFT) studies were carried out using the *Gaussian 16 software*, providing valuable insights into the structural and molecular properties of the compound studied [46]. These calculations play a crucial role in rational drug design by predicting physicochemical properties linked to biological activity and optimizing compounds for desired biomolecular interactions. Geometry optimization at the APFD/6–311G++(d,p) level confirmed a stable structure, indicated by the absence of negative frequencies. The methodology for evaluating stability and reactivity followed the approach described in the literature [47], with additional calculations performed to determine frontier molecular orbitals (HOMO and LUMO) and molecular electrostatic potential (MEP) using *Gauss View software* [48]. MEP visualization helps identify reactive sites, with red regions indicating electrophilic reactivity and blue regions highlighting nucleophilic reactivity.

#### 3.3. Docking studies

The chorioallantoic membrane (CAM) assay plays a critical role in evaluating the angioinhibitory effects of compounds. Molecular docking has become an essential computational technique for studying the interactions between candidate drugs and target proteins, predicting binding modes, and estimating binding affinities. Computer-aided molecular docking (CAMD) provides a robust in-silico method to assess the inhibitory potential of compounds targeting the deregulation of c-Met receptor tyrosine kinase activity. This approach allows for preliminary analysis of ligand-receptor interactions and binding affinity predictions. The kinase domain of the c-Met receptor was selected for docking studies, as it plays a critical role in angiogenesis and is a well-established therapeutic target for cancer treatment. Protein crystal structures of novel Class II c-Met inhibitors were obtained from the Protein Data Bank (PDB), specifically using the structure with PDB ID: 3U6J. The corresponding atomic coordinates file (.pdb format) was processed in Auto-Dock 4.2.6 software, part of the MGLTools suite [49]. Protein preparation involved removing water molecules and irrelevant ligands or ions, adding polar hydrogen atoms, assigning Kollman charges, and defining a grid box around the active site. The prepared protein file was then saved in .pdbqt format. Docking analysis were performed using AutoDock Vina, which calculates docking scores to estimate the binding affinity between ligands and receptors. Visualization and analysis of the docking results were carried out using Discovery Studio software, enabling a detailed interpretation of ligand-receptor interactions. Theoretical pKd values were calculated from docking-derived binding energies ( $\Delta G$ ) using the standard thermodynamic equation, assuming ideal conditions at 298 K [50].

#### 4. Results and discussion

#### 4.1. Chemistry

In the search for new potent anti-angiogenic small molecules, a series of thiophene-tethered pyrazoline derivatives (5a-h) were synthesized via a green, one-pot cyclocondensation approach. The key intermediate chalcone (3) was obtained through a base-catalyzed Claisen-Schmidt condensation between 2-formylthiophene (1) and acetone (2), producing an  $\alpha,\beta$ -unsaturated ketone. This intermediate then underwent cyclocondensation with various substituted phenylhydrazine hydrochlorides (4a-h) in methanol under reflux conditions. Citrus fruit juice, specifically extracted from Citrus aurantiifolia, played a dual role as both solvent and catalyst. Rich in organic acids-primarily citric acid-it provided a mildly acidic medium that facilitated the cyclization of chalcone with phenylhydrazines. The proposed mechanism, illustrated in Supplementary Figure S14, involves acid-catalyzed protonation of the chalcone's carbonyl group, increasing its electrophilicity and enabling nucleophilic attack by the hydrazine, followed by intramolecular ring closure and pyrazoline formation. Tetrabutylammonium bromide (TBAB) was employed as a phase-transfer catalyst to improve reaction efficiency. Reactions proceeded smoothly at 60–65 °C for approximately 4 h, affording the desired products in excellent yields (72-89 %). The use of citrus juice aligns with green chemistry principles, offering an ecofriendly, sustainable alternative to conventional acid catalysts. Structural confirmation of the synthesized compounds was achieved through <sup>1</sup>H NMR, <sup>13</sup>C NMR, and mass spectrometry. Notably, the disappearance of vinylic proton signals and the appearance of methylene proton resonances provided clear evidence for successful pyrazoline ring formation. A schematic representation of the synthetic route is shown in Scheme 1. The chemical structures of the synthesized compounds (5a-h) are provided in Supplementary Figure S1.

#### 4.2. Single crystal structural analysis

The single-crystal X-ray structure of compound 5 g (Fig. 3) reveals

Scheme 1. Syntheis of thiophene tethered pyrazolines, 5(a-h).

that the pyrazoline ring is bonded to two thiophene rings and a benzonitrile ring. The dihedral angle between the pyrazoline and benzonitrile rings is 6.78°, indicating near coplanarity. One thiophene ring,

connected via two carbon atoms to the pyrazoline ring, shows a dihedral angle of 10.77°, suggesting slight non-planarity. In contrast, the second thiophene ring, directly attached to the pyrazoline ring, adopts an almost perpendicular orientation with a dihedral angle of  $88.6^{\circ}$ (Figure S2). This spatial arrangement induces puckering in the pyrazoline ring, with a puckering amplitude (P) of 302.4(3)° and an asymmetry parameter  $\tau(M)$  of 20.8(1)°, consistent with an envelope conformation centered at the C10 atom (Figure S3). Supramolecular interactions play a key role in crystal stabilization. Notably, a C15-H15...N25 hydrogen bond [3.398(6) Å, 135.8(3)°, symmetry code:½ + x,  $\frac{1}{2}$  - y, - $\frac{1}{2}$  + z] forms an  $R_2^2(23)$  ring synthon. These motifs are further extended into a one-dimensional (1D) chain via C17-H17···N25 interactions (Fig. 4a), which then assemble into a two-dimensional (2D) supramolecular network through identical C17-H17···N25 linkages [3.398(6) Å, 144.0°, symmetry code:  $\frac{1}{2} + x$ ,  $\frac{1}{2} - y$ ,  $-\frac{1}{2} + z$ ] (Fig. 4b). In addition to hydrogen bonding, weak C—H···π (C—H···Cg) interactions significantly contribute to the crystal packing, as summarized in Table S1. Among these, the shortest distance was observed for the C3-H3···Cg2 interaction at 3.767(5) Å, followed by C3-H3···Cg4 at 3.795 (12) Å. Other notable contacts include C22-H22···Cg1 and C22-H22···Cg3, with distances of 3.578(3) Å and 3.521(18) Å, respectively.

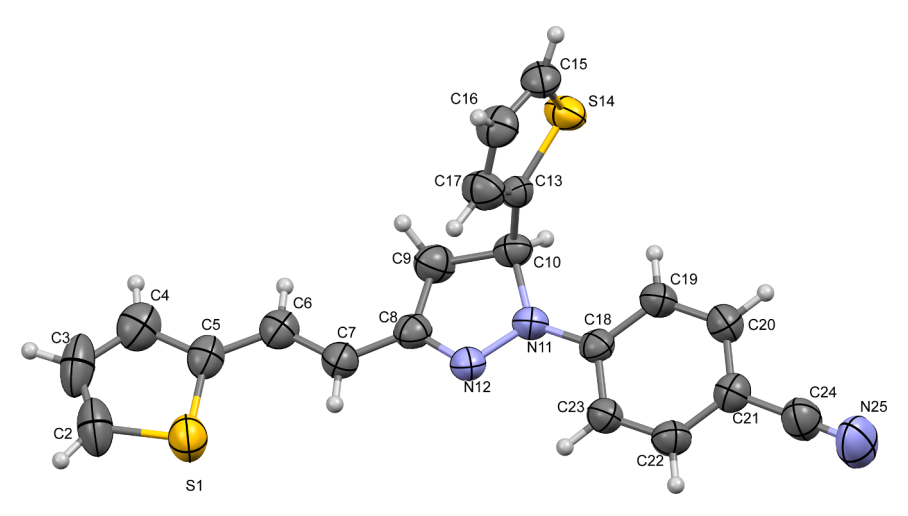


Fig. 3. The thermal ellipsoidal plot of the compound (5 g) along with the atom number scheme.

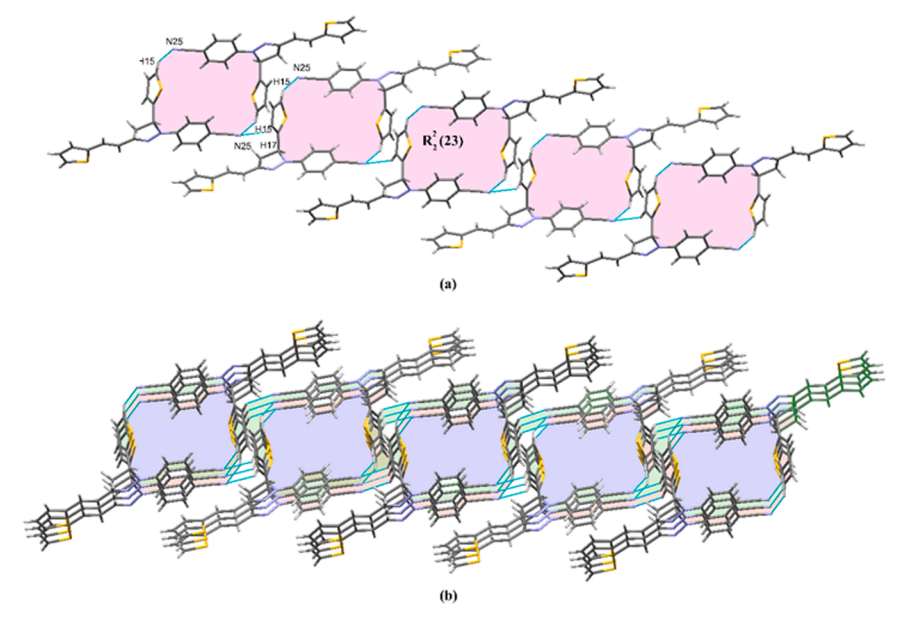


Fig. 4. The 1D and 2D architecture are formed by various interactions.

These non-covalent interactions collectively stabilize the 3D crystal lattice.

#### 4.3. Hirshfeld surface analysis

Hirshfeld surface analysis has emerged as a powerful tool in crystallography that quantifies and visualizes intermolecular interactions within crystals by analyzing the electron density distribution around each molecule. This analysis not only provides a quantitative fingerprint of these interactions through Fingerprint (FP) plots but also offers a visually informative 3D representation of the molecular size and shape. The  $d_{norm}$  Hirshfeld surface reveals two prominent red spots around N25, corresponding to interactions involving the C15-H15 and C17-H17 atoms (Fig. 5(a)). These regions of localized electron density highlight strong intermolecular interactions near the nitrogen atoms. The "bowtie" pattern of red and blue triangles around the thiophene ring indicates C—H··· $\pi$  stacking interactions, supported by the curvedness surface, which shows fewer blue lines around the thiophene ring (Fig. 5(b,c)). Additionally, the curvedness surface suggests a more coplanar molecular geometry, evidenced by the increased presence of blue lines (Fig. 5(c)).

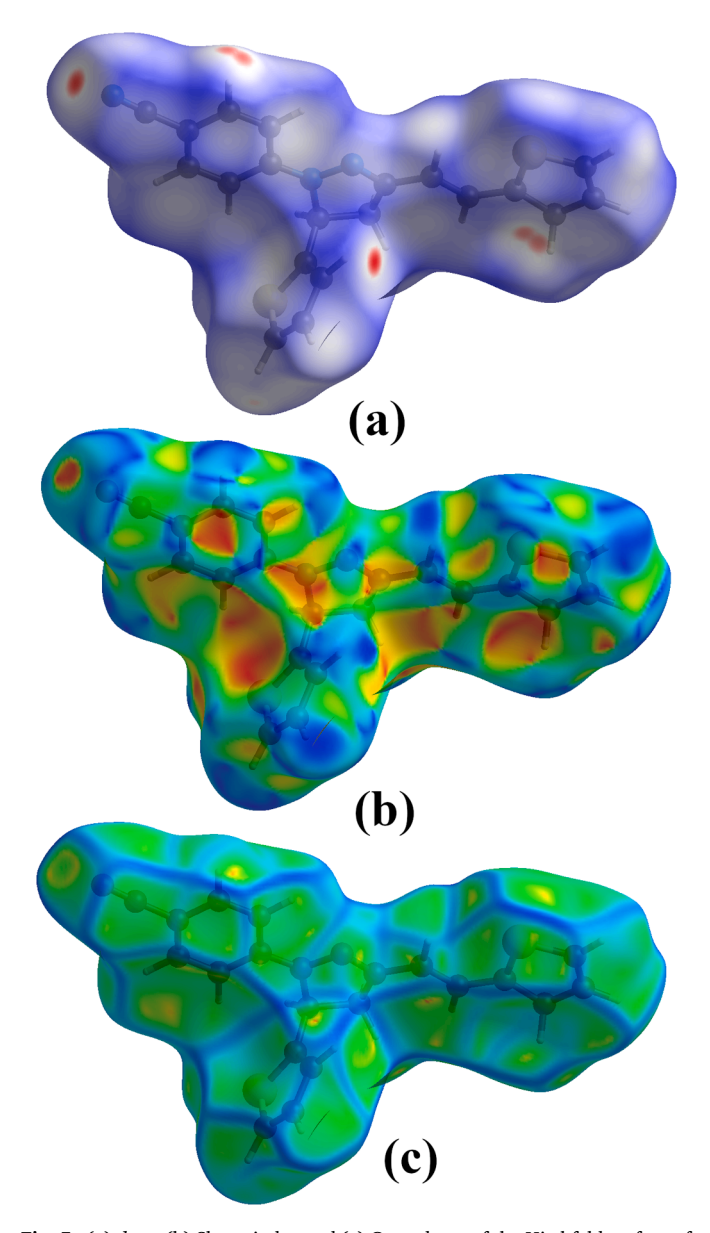


Fig. 5. (a)  $d_{\text{norm}}$  (b) Shape-index and (c) Curvedness of the Hirshfeld surface of the molecule.

The 2D fingerprint plot highlights the nature of intermolecular interactions within the crystal structure. H···H interactions dominate, accounting for 37.5 % of the contacts, represented by a broad peak centered around  $d_i{=}d_e{\approx}1.2$  Å, indicating strong hydrogen-hydrogen interactions (Fig. 6). C···H interactions, comprising 25.0 %, appear as wing-shaped peaks at  $d_i{+}d_e \geq 2.6$  Å, making them the second most prevalent interaction. H···N contacts (16 %) are depicted as sharp peaks at  $d_i{+}d_e \geq 2.4$  Å, while S···H interactions (13.8 %) create a distinct pattern resembling two inverted, opposing pigeons with characteristic peaks at  $d_i{+}d_e \geq 2.9$  Å. This analysis underscores that hydrogen-based interactions are the primary contributors to stabilizing the molecular packing.

The strength of crystal packing plays a crucial role in determining its response to external mechanical forces. If the packing contains significant voids, the molecules are loosely arranged, making the crystal more susceptible to breakage under minimal external pressure. To assess the mechanical stability, a void analysis was conducted by summing the electron densities of the spherically symmetric atoms present in the asymmetric unit. The void surface is defined as an isosurface of the procrystal electron density and is calculated across the entire unit cell. The void surface intersects the unit cell boundary, and capping faces are generated to form a closed volume of 216.20 ų (Figure S4). These results suggest that the crystal has a compact packing arrangement and should exhibit significant mechanical stability.

To gain a deeper understanding of the driving forces involved in crystal packing, the analysis of the surrounding environment of specific molecular fragments was conducted using energy framework analysis. This approach provides details of strongly bonded molecular fragments in the crystalline phase, focusing on molecule-molecule interactions. The total interaction energy for molecules within a 3.8 Å sphere was calculated (Table S2). The table presents interaction energy components for various symmetry-related molecular interactions, including electrostatic, polarization, dispersion, and repulsion energies. The most stabilizing interaction occurs at a distance of 10.65 Å, with the lowest total energy of -41.7 kJ/mol, indicating strong molecular attraction. The highest contribution from dispersion energy is -41.2 kJ/mol, observed at 11.14 Å, signifying that London dispersion forces play a crucial role in stabilization. Electrostatic interactions are most prominent at 11.52 Å, where the energy reaches -18.9 kJ/mol, reflecting strong charge-based interactions. However, steric repulsion is highest at 10.92 Å, with a repulsion energy of 18.4 kJ/mol, indicating significant hindrance in this interaction. Overall, dispersion energy (-249.8 kJ/ mol) is the dominant stabilizing factor, followed by electrostatic energy (-81.7 kJ/mol). Despite minor repulsion, the total interaction energy of -240.9 kJ/mol underscores the thermodynamic favorability of the packing arrangement (Fig. 7).

#### 4.4. Density functional theory studies

The optimized ground state energy of the studied compounds ranges from -1638.82 Hartree (compound 5a) to -4212.177 Hartree (compound 5f), indicating that 5f is the most electronically stable molecule in the series, while 5a is the least stable. The frontier molecular orbital (FMO) analysis reveals that the HOMO energy of -5.5604 eV reflects a moderate electron donating ability, which lies within the observed range of -5.6586 eV (5 g) to -4.9911 eV (5h). Similarly, the LUMO energy of -2.3709 eV is within the range of -2.2803 eV (5 g) to -1.8196 eV (5h), suggesting a moderate tendency to accept electrons. These values indicate a balanced electronic distribution, contributing to the moderate reactivity of the compounds. The HOMO-LUMO energy gap of 3.3789 eV for compound 5 g (Fig. 8) lies within the range of 3.1715 eV (5h) to 3.4578 eV (5b), confirming moderate electronic stability. Compound 5h, with the lowest energy gap, is expected to be the most chemically reactive, while 5b, with the highest gap, is the most stable and least reactive. Ionization energy (I) and electron affinity (A) values also support this trend. The ionization energy of 5.5604 eV and electron

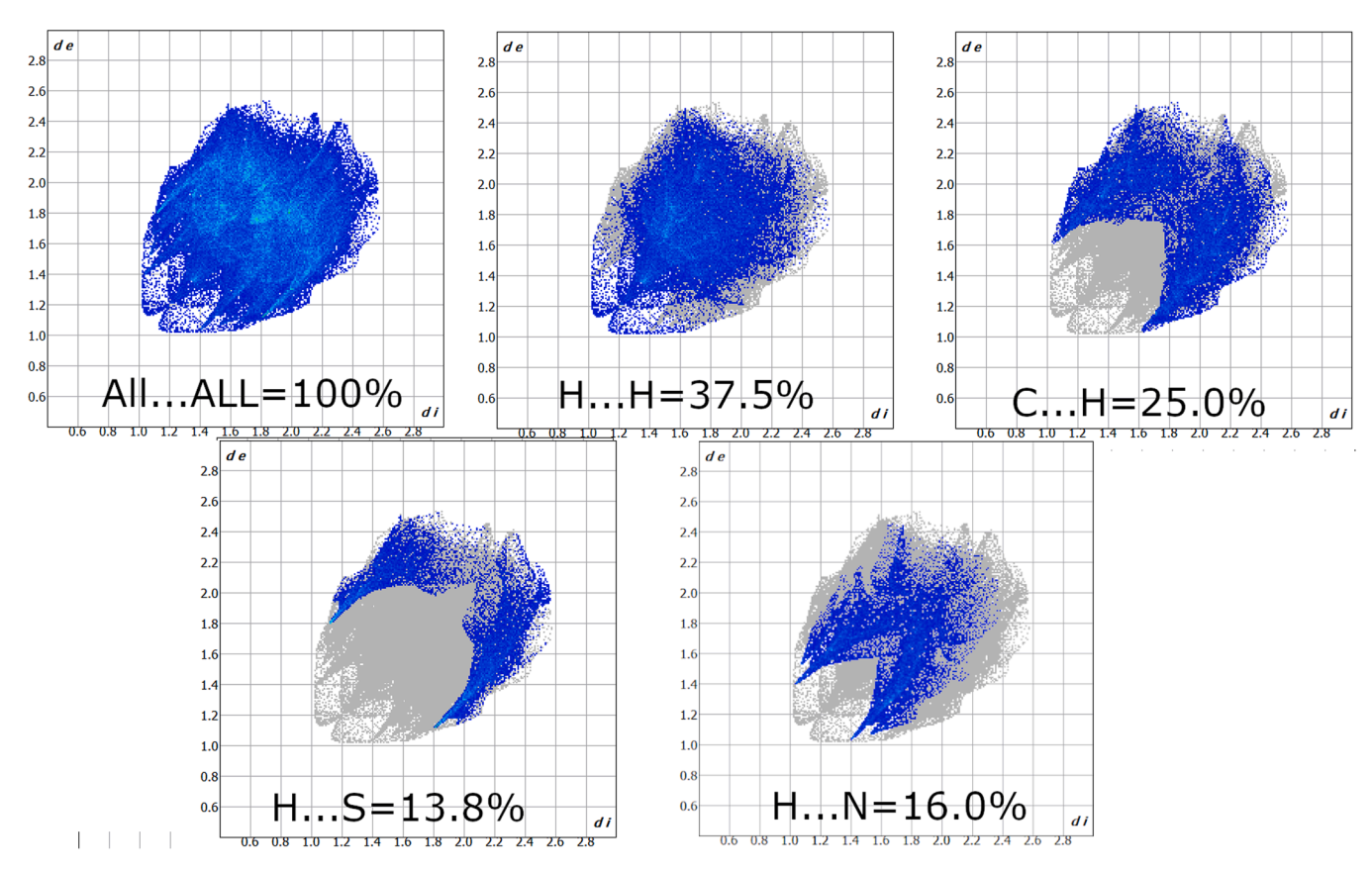


Fig. 6. 2D Fingerprint plots and corresponding surface area of the title compound 5 g showing the individual contribution of each interaction.

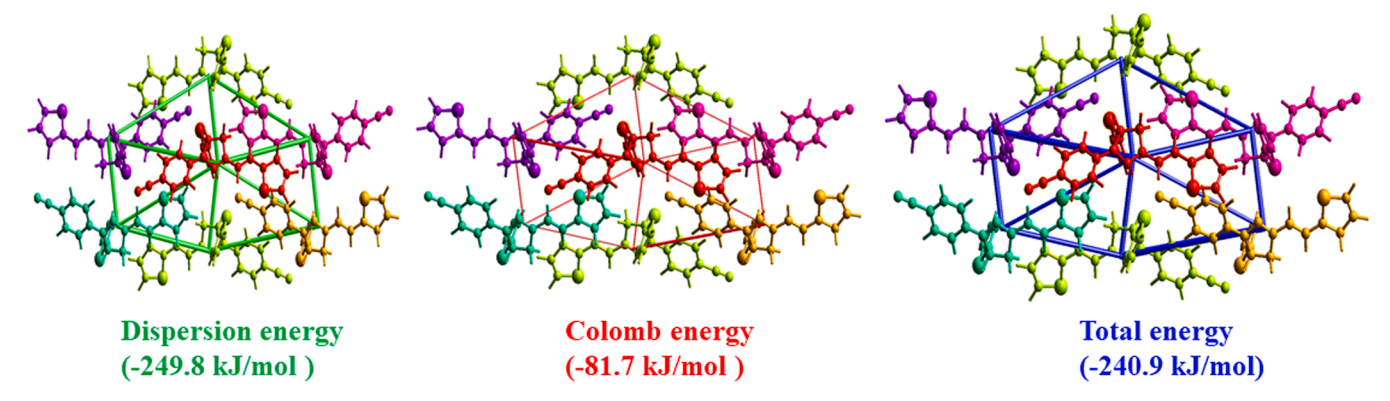


Fig. 7. The energy framework table along with interaction energy.

affinity of 2.3709 eV fall within the ranges observed across the series (I: 4.9911–5.6586 eV; A: 1.8196–2.2803 eV), reflecting the compounds' moderate electron donating and accepting capabilities.

Global reactivity descriptors further validate these findings. The electronegativity ( $\chi$ ) of 3.9657 eV and chemical potential ( $\mu$ ) of –3.9657 eV fall within the ranges of 3.4054–3.9695 eV and –3.4054 to –3.9695 eV, respectively. The global hardness ( $\eta$ ) of 1.5947 eV is within the expected range of 1.5857–1.7289 eV, indicating moderate resistance to charge transfer. The electrophilicity index ( $\omega$ ) of 4.9308 eV is consistent with values from 3.6565 eV (**5h**) to 4.6641 eV (**5 g**), highlighting the compounds' potential to act as electron acceptors. Overall, compound **5h** is the most reactive due to its low energy gap, low ionization energy, and high electron affinity, whereas **5b** appears the least reactive based on its wider gap and higher global hardness.

Molecular electrostatic potential (MEP) maps provide insight into the charge distribution and reactive regions of the molecules. Compound **5a** exhibits a relatively narrow potential range (-0.0311 to +0.0311 a. u.), while **5h** demonstrates the broadest variation (-0.0622 to +0.062 a. u.), indicating a clear separation of nucleophilic and electrophilic regions. Compound 5e shows the highest polarity, with values of approximately  $\pm 0.0316$  a.u., which may favor nucleophilic interactions. A symmetrical charge distribution is observed in compound 5f, with potentials around  $\pm 0.0322$  a.u. The high negative potential regions typically correspond to the nitrogen atoms of the pyrazoline ring, indicating nucleophilic character, while positive potentials near C-H groups suggest electrophilic behavior. Additionally, halogen atoms and OCH3 substituents in compound 5h, along with the -C=N group in 5 g (Fig. 9), contribute to enhanced nucleophilicity in specific regions of the molecular surface. A good structural correlation between the optimized and experimental crystal geometries is confirmed by an RMSD value of 0.416 Å (Figure S5). Further, Tables S1-S3 show strong agreement in bond lengths, angles, and torsional parameters, reinforcing the reliability of

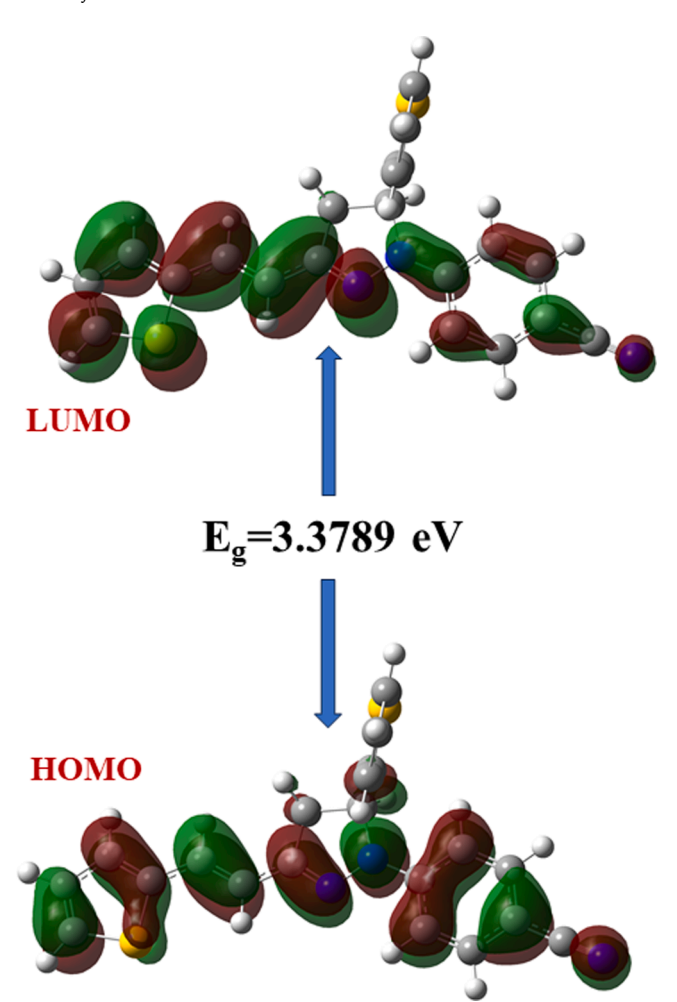


Fig. 8. The HOMO-LUMO energy gap of the Compound 5 g.

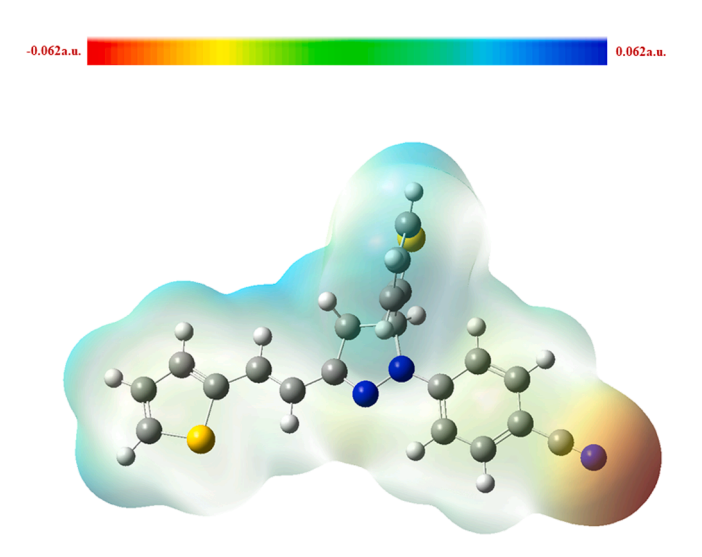


Fig. 9. MEP of the compound 5 g.

the DFT models. Optimized geometries of all synthesized compounds (5a–5h) are provided in Supplementary Figures S6–S12.

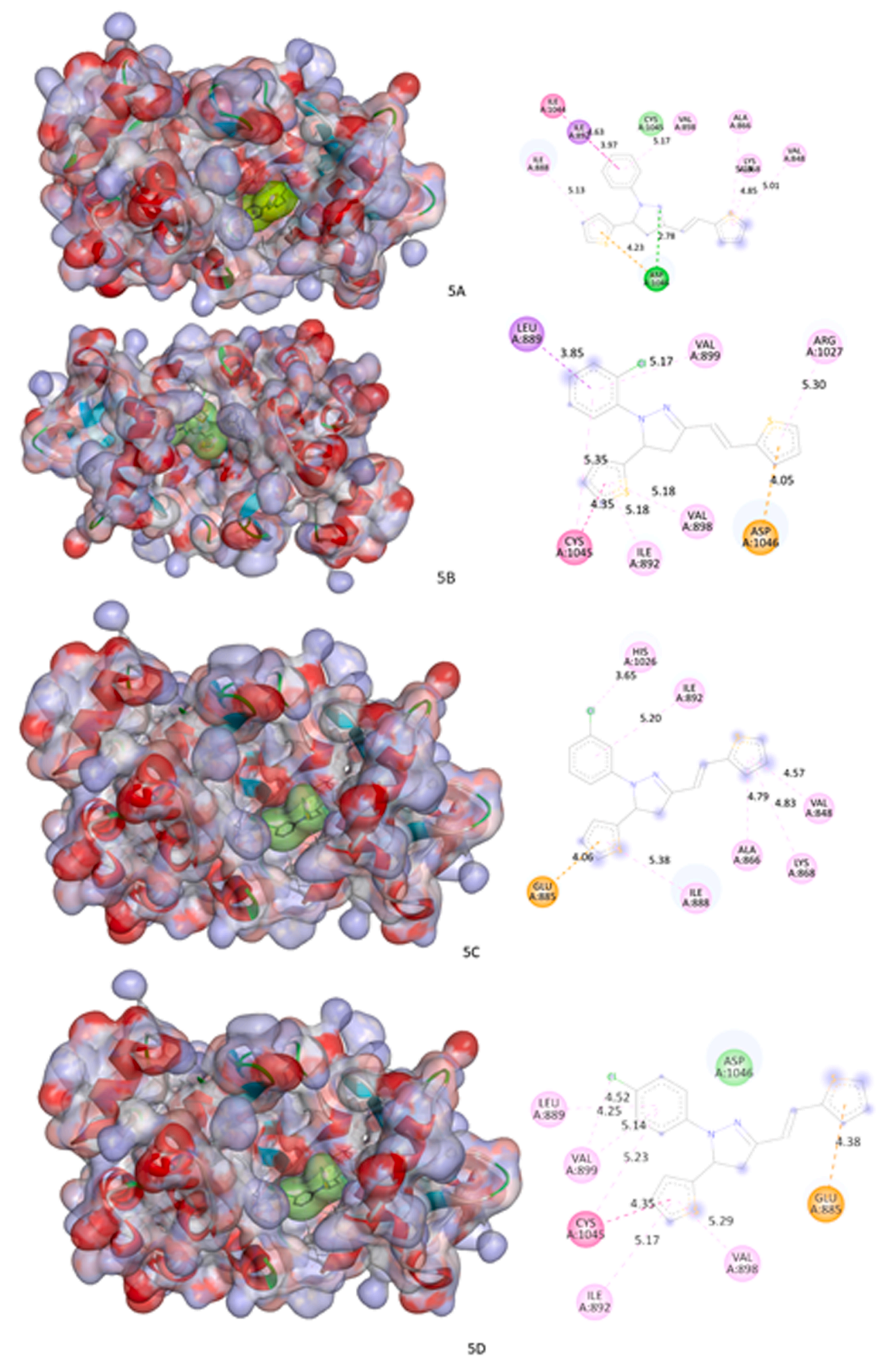
#### 4.5. Angioinhibitory effect by chorioallantoic membrane (CAM) assay

The chorioallantoic membrane (CAM) assay was employed to

evaluate the anti-angiogenic activity of the synthesized thiophenetethered pyrazoline derivatives (5a-h), with representative results illustrated in Figures S13-S14. This assay serves as a physiologically relevant in vivo model to assess the ability of compounds to inhibit new blood vessel formation-a critical process in tumor progression and metastasis. Among the tested series, compounds 5a, 5c, 5 g, and 5h exhibited the most potent anti-angiogenic activity, as evidenced by a marked reduction in capillary proliferation around the compoundloaded discs. The experiment was conducted using a minimum of six fertilized eggs per treatment group to ensure statistical reliability. Compared to the saline-treated control group, which displayed extensive vasculature due to unimpeded angiogenesis, the treated groups demonstrated a significant decrease in microvessel density, indicating the compounds' ability to suppress neovascularization. This observed anti-angiogenic effect is of substantial therapeutic interest, as angiogenesis is essential for tumor survival, growth, and metastatic spread. By inhibiting the development of new capillaries, these compounds potentially starve tumor cells of the oxygen and nutrients required for sustained proliferation. The results not only confirm the biological relevance of the synthesized molecules but also underscore their potential as anti-cancer agents targeting tumor vasculature. Importantly, the experimental findings align with the molecular docking data, which predict favorable interactions between the compounds and c-Met, a receptor tyrosine kinase implicated in angiogenesis. The regression in microvessel density in the CAM model strongly suggests the inhibition of angiogenesis, while the docking results provide a molecular basis for this effect by demonstrating potential binding interactions with key angiogenic targets. Collectively, these in vivo and in silico insights reinforce the therapeutic promise of the thiophene-tethered pyrazoline derivatives as viable lead candidates in the development of anti-angiogenic agents.

#### 4.6. Docking studies

Molecular docking serves as a pivotal tool in medicinal chemistry, enabling the prediction and understanding of ligand-protein interactions, thereby facilitating the development of targeted therapeutic agents. To investigate the potential of the synthesized thiophenetethered pyrazoline derivatives (5a-h) as inhibitors of the c-Met receptor tyrosine kinase, docking studies were conducted using the c-Met protein structure (PDB ID: 3U6J). Figs. 10-11 illustrate the 3D and 2D docking poses of these pyrazoline derivatives within the c-Met binding site. The most favorable docking scores ranged from -6.7 to -9.1 kcal/ mol, attributed to key interactions with amino acid residues via  $\pi$ - $\pi$ stacking, π-based contacts, hydrogen bonding, and van der Waals forces, as summarized in **Table S4**. To support the relevance of the docking site and provide a biologically validated reference, we used the pyrazolonebased compound co-crystallized in the kinase domain of the c-Met receptor as a structural benchmark. Although we did not redock the reference inhibitor, its binding conformation helped define the active site, and the observed docking scores of our pyrazoline derivatives were within a comparable range, suggesting similar binding potential. Among the compounds, 5c demonstrated the highest docking score of -9.1kcal/mol, suggesting the strongest predicted binding affinity and positioning it as a potentially more effective inhibitor of the c-Met receptor. Compound 5a, with a docking score of -8.9 kcal/mol, also exhibited strong binding, similar to 5c but slightly weaker. Compounds 5b (-8.6 kcal/mol) and 5 g (-9.0 kcal/mol) showed favorable binding, further supporting their inhibitory potential. The docking scores for 5d and 5e (both -8.2 kcal/mol) suggest moderate affinity, while compound 5f, with the lowest score of -6.7 kcal/mol, indicates a weaker interaction but still within an acceptable range for a potential inhibitor. To quantify the binding affinities of these pyrazoline derivatives, theoretical pKd values were calculated from the docking scores using the standard thermodynamic relationship between binding free energy and dissociation constant, These values which reflect the predicted strength of



 $\textbf{Fig. 10.} \ \ \textbf{3D} \ \ \textbf{and 2D} \ \ \textbf{binding interactions of pyrazoline derivatives (5a-d) at the binding site.}$ 

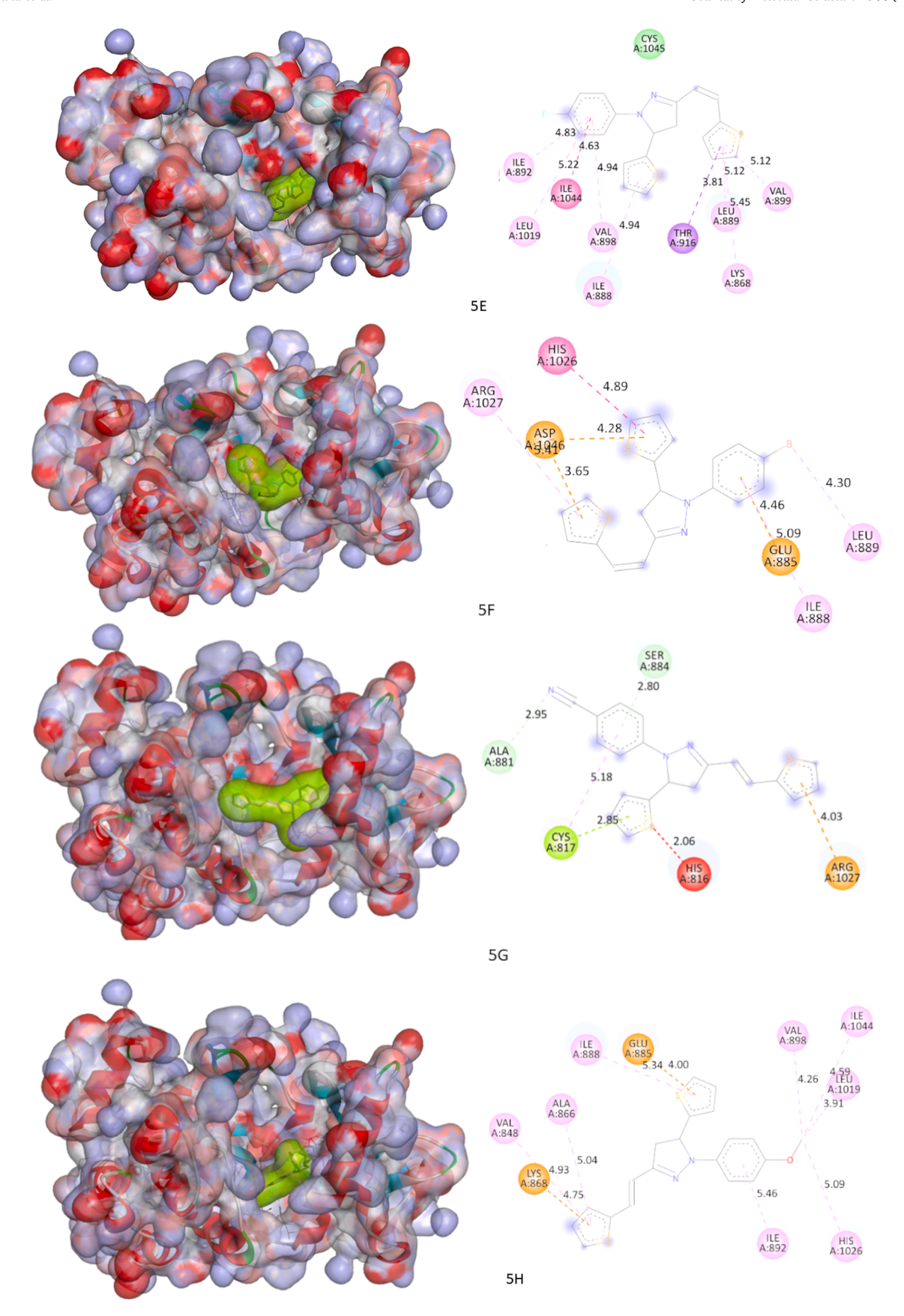


Fig. 11. 3D and 2D binding interactions of pyrazoline derivatives (5e-h) at the binding site.

binding to the c-Met receptor, ranged from 4.93 to 6.68. Notably, Compound 5c, with the highest pKd value of 6.68, showed the strongest predicted binding affinity, further supporting its potential as a competitive c-Met receptor inhibitor. Specifically, compound 5a demonstrated a strong hydrogen bond interaction between the centroid of the pyrazoline ring and the amino acid Asp1046 at a distance of 2.78 Å. Additionally, the benzonitrile ring attached to the pyrazoline moiety in compound 5 g formed two van der Waals interactions with the amino acids Ser884 and Ala881 at distances of 2.80 Å and 2.95 Å, respectively, along with a significant hydrogen bond interaction with amino acid Cys817 at a distance of 2.85 Å. Furthermore, halogen atoms present in compounds 5c and 5d were observed to interact with amino acids His1026 and Val899 within the c-Met binding site, enhancing the binding affinity of these compounds. The amino acid Val898 prominently displayed  $\pi$ - $\pi$  interactions with substituted pyrazolines (5a, 5b, and 5d), playing a significant role in enhancing their binding affinity. Collectively, the docking studies and the calculated pKd values, provided in Table S1, offer valuable insights into the binding modes and interactions of the pyrazoline derivatives with the c-Met receptor, supporting their potential as therapeutic agents targeting c-Met-mediated signaling pathways involved in tumor progression. The consistency between docking scores and biological activity further reinforces the relevance of these findings. Compounds 5a, 5c, 5 g, and 5h, which exhibited strong docking scores, also demonstrated notable antiangiogenic effects in the CAM assay. Compounds 5b, 5d, and 5e showed moderate effects, while compound 5f, which had the weakest docking score, showed minimal biological activity. This observed correlation highlights a structure-activity relationship (SAR), where electron-withdrawing groups (e.g., 3-chloro in 5c and 4-cyano in 5 g) enhanced both receptor binding and biological efficacy, whereas electron-donating groups like 4-methoxy in 5h yielded relatively lower docking scores and moderate activity. These observations underscore the importance of substituent effects in modulating bioactivity and support the predictive utility of docking for guiding future structural optimization.

#### 5. Conclusion

In conclusion, the docking studies and CAM assay demonstrate that the pyrazoline derivatives, particularly compounds 5a, 5c, 5 g, and 5 h, exhibit promising anti-angiogenic effects, with potential as competitive Class II c-Met inhibitors. The crystal structure of compound 5 g reveals a complex molecular arrangement, including thiophene and benzonitrile rings, with a sTable 2D supramolecular architecture formed through C-H...N interactions. The crystal exhibits strong mechanical stability due to its compact packing and minimal voids, while energy framework analysis reveals that dispersion and electrostatic interactions play key roles in stabilizing the structure. Despite steric repulsion, the overall interaction energy suggests a stable molecular arrangement. Hirshfeld surface analysis underscores the importance of hydrogen-based interactions in stabilizing the crystal structure, with H···H, C···H, H···N, and S···H interactions being predominant. Additionally, the molecule's moderate reactivity, as indicated by its energy gap, ionization energy, and electron affinity, supports its balanced electrophilic and nucleophilic nature. Compound 5 g exhibits moderate reactivity, stability, and electron transfer properties, with values consistently aligning with observed ranges across various compounds. The analysis of ionization energy, electron affinity, and energy gap highlights the varying reactivity among compounds, with 5h showing the highest reactivity and 5b the lowest. The electrostatic potential maps further confirm these trends, indicating distinct electrophilic and nucleophilic regions across the different compounds. The MEP map provides further insight into its potential for intermolecular interactions, suggesting a promising pathway for developing effective therapeutic agents targeting angiogenesis. Notably, these compounds were synthesized via an innovative and eco-friendly green protocol using citrus extract for the

cyclocondensation of thienyl chalcone with phenylhydrazine hydrochlorides, offering a sustainable alternative to conventional acid-catalyzed methods. Collectively, these findings underscore the promise of these pyrazoline derivatives as lead candidates for the development of anti-angiogenic agents targeting angiogenesis in cancer therapy.

#### CRediT authorship contribution statement

Chandan Mallikarjuna: Writing – review & editing, Writing – original draft, Validation, Methodology, Data curation. Udaya Kumar A H: Visualization, Validation, Software, Data curation. Mahesha: Validation, Software, Data curation. Rekha N Dharmappa: Visualization, Validation, Software, Data curation. Deepashree Nagaraj: Visualization, Validation, Software. Neratur Krishnappagowda Lokanath: Supervision, Software, Investigation, Conceptualization. Kariyappa Ajay Kumar: Writing – review & editing, Writing – original draft, Supervision, Methodology, Investigation, Conceptualization.

#### Declaration of competing interest

The authors declare that they have no known competing financial interests or personal relationships that could have appeared to influence the work reported in this paper.

#### Acknowledgements

The authors are grateful to the National Single Crystal Diffractometer Facility, Department of Studies in Physics, University of Mysore, for the X-ray diffraction studies, and to the USIC, JSS Academy of Higher Education and Research (JSS University), for recording the spectra.

#### Supplementary materials

Supplementary material associated with this article can be found, in the online version, at doi:10.1016/j.molstruc.2025.142959.

#### Data availability

The data that has been used is confidential.

#### References

- [1] A.D. Kumar, H.K. Vivek, B. Srinivasan, S. Naveen, K. Kumara, N.K. Lokanath, K. Byrappa, K.A. Kumar, Design, synthesis, characterization, crystal structure, Hirshfeld surface analysis, DFT calculations, anticancer, angiogenic properties of new pyrazole carboxamide derivatives, J. Mol. Struct. 1235 (2021) 130271, https://doi.org/10.1016/j.molstruc.2021.130271.
- [2] Z. Wang, C. Dabrosin, X. Yin, M.M. Fuster, A. Arreola, W.K. Rathmell, D. Generali, G.P. Nagaraju, B. El-Rayes, D. Ribatti, Y.C. Chen, K. Honoki, H. Fujii, A. G. Georgakilas, S. Nowsheen, A. Amedei, E. Niccolai, A. Amin, S.S. Ashraf, B. Helferich, X. Yang, G. Guha, D. Bhakta, M.R. Ciriolo, K. Aquilano, S. Chen, D. Halicka, S.I. Mohammed, A.S. Azmi, A. Bilsland, W.N. Keith, L.D. Jensen, Broad targeting of angiogenesis for cancer prevention and therapy, Semin. Cancer Biol. 35 (2015) S224–S243, https://doi.org/10.1016/j.semcancer.2015.01.001.
- [3] Y.U. Cao, Z.D. Fu, F. Wang, H.Y. Liu, R.U.I. Han, Anti-angiogenic activity of resveratrol, a natural compound from medicinal plants, J. Asian Nat. Prod. Res. 7 (3) (2005) 205–213.
- [4] S. Tugues, S. Koch, L. Gualandi, X. Li, L. Claesson-Welsh, Vascular endothelial growth factors and receptors: anti-angiogenic therapy in the treatment of cancer, Mol. Asp. Med. 32 (2) (2011) 88–111, https://doi.org/10.1016/j. mam.2011.04.004.
- [5] Z.M. Alamshany, E.M. Algamdi, I.M. Othman, M.M. Anwar, E.S. Nossier, New Pyrazolopyridine and Pyrazolothiazole-Based Compounds As Anti-Proliferative Agents Targeting C-Met Kinase inhibition: design, synthesis, Biological evaluation, and Computational Studies, 13, RSC advances, 2023, pp. 12889–12905.
- [6] W. Auerbach, R. Auerbach, Angiogenesis Inhibition: a review, Pharmacol. Ther. 63 (3) (1994) 265–311, https://doi.org/10.1016/0163-7258(94)90027-2.
- [7] K.M. Kasiotis, E.N. Tzanetou, S.A. Haroutounian, Pyrazoles as potential antiangiogenesis agents: a contemporary overview, Front. Chem. 2 (2014), https://doi. org/10.3389/fchem.2014.00078.
- [8] K. Karrouchi, S. Radi, Y. Ramli, J. Taoufik, Y.N. Mabkhot, F.A. Al-aizari, M. Ansar, Synthesis and pharmacological activities of pyrazole derivatives: a review, Molecules 23 (1) (2018) 134, https://doi.org/10.3390/molecules23010134.

- [9] Y.N. Mabkhot, F. Alatibi, A. Barakat, S.S. Al-Showiman, R. Al-Salahi, Synthesis and anticancer evaluation of new thiophene derivatives, J. Chem. (2020), https://doi. org/10.1155/2020/8856039. 2020, Article ID 8856039.
- [10] R. Kumar, G. Sahoo, A. Dey, D. Nayak, Biological potential and synthetic strategies of pyrazole derivatives: a recent update, Molecules 28 (16) (2023) 6055, https:// doi.org/10.3390/molecules28166055.
- [11] G.M. Edrees, H.I. El-Subbagh, M.A. El-Sayed, Thiophene-based N-phenyl pyrazolines: synthesis, anticancer activity, molecular docking and ADME study, J. Appl. Pharm. Sci. 10 (6) (2020) 35–42, https://doi.org/10.7324/ JAPS.2020.10606.
- [12] Y.N. Nayak, S. Pandey, S.R. Pai, N.S. Gandhi, R. Nayak, Z. Xi, V. Pandey, B. Basappa, S.L. Gaonkar, Design, synthesis, In Silico analysis, anti-inflammatory, and cytotoxicity evaluation of Novel Formyl-Pyrazoline derivatives, J. Mol. Struct. 1324 (2025) 140821, https://doi.org/10.1016/j.molstruc.2024.140821.
- [13] K. Rouzi, S. Mortada, M. Hassan, A. Alsalme, A. Kloczkowski, M.E. Karbane, M. Bouatia, M.E.A. Faouzi, K. Karrouchi, Novel 3,5-dimethylpyrazole-linked 1,2,4triazole-3-thiols as potent antihyperglycemic agents: synthesis, biological evaluation, and In Silico molecular modelling investigations, ChemistrySelect 9 (37) (2024) e202403661, https://doi.org/10.1002/slct.202403661.
- [14] B. Kurban, B.N. Sağlık, D. Osmaniye, S. Levent, Y. Özkay, Z.A. Kaplancıklı, Synthesis and anticancer activities of Pyrazole–Thiadiazole-based EGFR inhibitors, ACS Omega 8 (34) (2023) 31500–31509, https://doi.org/10.1021/ acsomega.304635.
- [15] P.M. Uppar, K.K. Harish, N.M. Beeraka, Z. Xi, C. Somu, M. Madegowda, M. S. Kempasiddegowda, S.M. Parameshwaraiah, P.E. Lobie, K.S. Rangappa, V. Pandey, B. Basappa, Optimizing adamantane derivatives for enhanced EGFR inhibition in MCF-7 breast cancer cells, J. Mol. Struct. 1331 (2025) 141554, https://doi.org/10.1016/j.molstruc.2025.141554.
- [16] E.O. Hamed, M.G. Assy, N.H. Ouf, D.A. Elsayed, M.H. Abdellattif, Cyclization of N-acetyl derivative: novel synthesis Azoles and azines, antimicrobial activities, and computational studies, Heterocycl. Comm. 28 (1) (2022) 35–43, https://doi.org/10.1515/hc-2022-0004.
- [17] A.T. Shaw, D.-W. Kim, K. Nakagawa, T. Seto, L. Crinó, M.-J. Ahn, T. De Pas, B. Besse, B.J. Solomon, F. Blackhall, Y.-L. Wu, M. Thomas, K.J. O'Byrne, D. Moro-Sibilot, D.R. Camidge, T. Mok, V. Hirsh, G.J. Riely, S. Iyer, V. Tassell, A. Polli, K. D. Wilner, P.A. Jänne, Crizotinib versus chemotherapy in advanced ALK -positive lung cancer, N. Engl. J. Med. 368 (25) (2013) 2385–2394, https://doi.org/10.1056/NEJMoa1214886.
- [18] M.E. Ganapathy, W. Huang, D.P. Rajan, A.L. Carter, M. Sugawara, K. Iseki, F. H. Leibach, V. Ganapathy, β-lactam antibiotics as substrates for OCTN2, an organic cation/carnitine transporter, J. Biol. Chem. 275 (3) (2000) 1699–1707, https://doi.org/10.1074/jbc.275.3.1699.
- [19] K. Karrouchi, S. Radi, Y. Ramli, J. Taoufik, Y.N. Mabkhot, F.A. Al-aizari, M. Ansar, Synthesis and pharmacological activities of pyrazole derivatives: a review, Molecules. 23 (1) (2018) 134, https://doi.org/10.3390/molecules23010134.
   [20] F.E. Bennani, L. Doudach, Y. Cherrah, Y. Ramli, K. Karrouchi, M. Ansar, M.E.
- [20] F.E. Bennani, L. Doudach, Y. Cherrah, Y. Ramli, K. Karrouchi, M. Ansar, M.E. A. Faouzi, Overview of recent developments of pyrazole derivatives as an anticancer agent in different cell line, Bioorg. Chem. 97 (2020) 103470, https://doi.org/10.1016/j.bioorg.2019.103470.
- [21] G. Dowling, E. Malone, Analytical strategy for the confirmatory analysis of the non-steroidal anti-inflammatory drugs Firocoxib, propyphenazone, Ramifenazone and Piroxicam in Bovine plasma by liquid chromatography tandem mass spectrometry, J. Pharm. Biomed. Anal. 56 (2) (2011) 359–365, https://doi.org/10.1016/j.jpha.2011.05.029.
- [22] M. Furia, L. Gianfreda, V. Scardi, Cellulase and related enzyme activities in a carnivorous mollusc: octopus Vulgaris Lamarck, Comp. Biochem. Physiol. B 52 (4) (1975) 529–532, https://doi.org/10.1016/0305-0491(75)90231-x.
- [23] J. Shallcross, P. Hámor, A.R. Bechard, M. Romano, L. Knackstedt, M. Schwendt, The divergent effects of CDPPB and cannabidiol on fear extinction and anxiety in a predator scent stress model of PTSD in rats, Front. Behav. Neurosci. 13 (2019) 91, https://doi.org/10.3389/fnbeh.2019.00091.
- [24] I.M. Spitz, B.H. Novis, R. Ebert, S. Trestian, D. LeRoith, W. Creutzfeldt, Betazole-induced GIP secretion is not mediated by gastric HCl, Metabolism 31 (4) (1982) 380–382, https://doi.org/10.1016/0026-0495(82)90114-7.
- [25] G. Luo, Y. Ma, X. Liang, G. Xie, Y. Luo, D. Zha, S. Wang, L. Yu, X. Zheng, W. Wu, C. Zhang, Design, synthesis and antitumor evaluation of novel 5-methylpyrazolo [1,5-a]pyrimidine derivatives as potential c-Met inhibitors, Bioorg. Chem. 104 (2020) 104356, https://doi.org/10.1016/j.bioorg.2020.104356.
- [26] E.A. Abdelsalam, A.A. Abd El-Hafeez, W.M. Eldehna, M.A. El Hassab, H.M. M. Marzouk, M.M. Elaasser, N.A. Abou Taleb, K.M. Amin, H.A. Abdel-Aziz, P. Ghosh, S.F. Hammad, Discovery of novel thiazolyl-pyrazolines as dual EGFR and VEGFR-2 inhibitors endowed with in vitro antitumor activity towards non-small lung cancer, J. Enzyme Inhib. Med. Chem. 37 (1) (2022) 2265–2282, https://doi.org/10.1080/14756366.2022.2104841.
- [27] M.G. Salem, M.S. Nafie, A.A. Elzamek, H.A. Elshihawy, M.A. Sofan, E. Negm, Design, synthesis, and biological investigations of new pyrazole derivatives as VEGFR2/CDK-2 inhibitors targeting liver cancer, BMC Chem. 18 (1) (2024) 208, https://doi.org/10.1186/s13065-024-01314-z.
- [28] I. Ameziane El Hassani, A. Altay, K. Karrouchi, E. Yeniçeri, B. Türkmenoğlu, H. Assila, Y. Boukharssa, Y. Ramli, M. Ansar, Novel pyrazole-based benzofuran derivatives as anticancer agents: synthesis, biological evaluation, and molecular

- docking investigations, Chem. Biodivers. 20 (11) (2023) e202301145, https://doi.org/10.1002/cbdv.202301145.
- [29] I. Ameziane El Hassani, S. Mortada, N.J. Gumede, H. Assila, A. Alsalme, A. Oulmidi, M.E.A. Faouzi, K. Karrouchi, M. Ansar, Design, synthesis, stereochemical characterization, in vitro α-glucosidase, and α-amylase inhibition and in silico studies of novel pyrazole-hydrazide hydrazones, Med. Chem. Res. 34 (1) (2025) 252–271, https://doi.org/10.1007/s00044-024-03335-8.
- [30] M. Elkolli, N. Chafai, S. Chafaa, I. Kadi, C. Bensouici, A. Hellal, New phosphinic and phosphonic acids: synthesis, antidiabetic, anti-alzheimer, antioxidant activity, DFT study and SARS-CoV-2 inhibition, J. Mol. Struct. 1268 (2022) 133701, https://doi.org/10.1016/j.molstruc.2022.133701.
- [31] H. Tlidjane, N. Chafai, S. Chafaa, C. Bensouici, K. Benbouguerra, New thiophenederived α-aminophosphonic acids: synthesis under microwave irradiations, antioxidant and antifungal activities, DFT investigations and SARS-CoV-2 main protease inhibition, J. Mol. Struct. 1250 (2022) 131853, https://doi.org/10.1016/ i.molstruc.2021.131853.
- [32] N. Houas, S. Chafaa, N. Chafai, S. Ghedjati, M. Djenane, S. Kitouni, Synthesis, characterization, DFT study and antioxidant activity of (2-hydroxynaphthalen-1-yl) methyl 2-hydroxyphenyl amino phosphonic acid, J. Mol. Struct. 1247 (2022) 131322, https://doi.org/10.1016/j.molstruc.2021.131322.
- [33] K. Benbouguerra, N. Chafai, S. Chafaa, Y.I. Touahria, H. Tlidjane, New α-hydrazinophosphonic acid: synthesis, characterization, DFT study and in silico prediction of its potential inhibition of SARS-CoV-2 main protease, J. Mol. Struct. 1239 (2021) 130480, https://doi.org/10.1016/j.molstruc.2021.130480.
- [34] S. Zaout, S. Chafaa, A. Hellal, O. Boukhemis, L. Khattabi, H. Merazig, N. Chafai, C. Bensouici, L. Bendjeddou, Hydroxyphenylamine phosphonate derivatives: synthesis, X-ray crystallographic analysis, and evaluation of theirs anti-alzheimer effects and antioxidant activities, J. Mol. Struct. 1225 (2021) 129121, https://doi. org/10.1016/j.molstruc.2020.129121.
- [35] C.B. Vagish, A. Dileep Kumar, K. Kumara, H.K. Vivek, N. Renuka, N.K. Lokanath, K. Ajay Kumar, Environmentally benign synthesis of substituted pyrazoles as potent antioxidant agents, characterization and docking studies, J. Iran. Chem. Soc. 18 (2) (2021) 479–493, https://doi.org/10.1007/s13738-020-02042-6.
- [36] N. Karki, H. Achhami, B.B. Pachhai, S. Bhattarai, D.K. Shahi, L.R. Bhatt, M.K. Joshi, Evaluating citrus juice: a comparative study of physicochemical, nutraceutical, antioxidant, and antimicrobial properties of citrus juices from Nepal, Heliyon 10 (23) (2024) e40773. https://doi.org/10.1016/j.heliyon.2024.e40773.
- (23) (2024) e40773, https://doi.org/10.1016/j.heliyon.2024.e40773.
   [37] N.D. Rekha, S.M. Aradhya, K. Jayashree, The antiangiogenic, antioxidant and proapoptotic chemopreventive properties of tannins from Memecylon malabaricum (Cl.), Int. J. Pharm. Sci. Res. (IJPSR) 6 (1) (2015) 259–266.
- [38] C.-S. Expert, Rigaku Corporation, Tokyo, Japan (2011).
- [39] G.M. Sheldrick, SHELXT–Integrated space-group and crystal-structure determination, Acta Crystallogr. A: Found. Adv. 71 (1) (2015) 3–8.
- [40] G.M. Sheldrick, SHELXT Integrated space-group and crystal-structure determination, Acta Crystallogr. Found. Adv. 71 (1) (2015) 3–8, https://doi.org/ 10.1107/S2053273314026370.
- [41] O.V. Dolomanov, L.J. Bourhis, R.J. Gildea, J.A.K. Howard, H. Puschmann, *OLEX2*: a complete structure solution, refinement and analysis program, J. Appl. Crystallogr. 42 (2) (2009) 339–341, https://doi.org/10.1107/S0021889808042726
- [42] A. Spek, PLATON, an integrated tool for the analysis of the results of a single crystal structure determination, Acta Crystallogr. A: Found. Crystallogr. 46 (s1) (1990) c34-c34
- [43] C.F. Macrae, I. Sovago, S.J. Cottrell, P.T.A. Galek, P. McCabe, E. Pidcock, M. Platings, G.P. Shields, J.S. Stevens, M. Towler, P.A. Wood, *Mercury 4.0*: from visualization to analysis, design and prediction, J. Appl. Crystallogr. 53 (1) (2020) 226–235, https://doi.org/10.1107/S1600576719014092.
- [44] P.R. Spackman, M.J. Turner, J.J. McKinnon, S.K. Wolff, D.J. Grimwood, D. Jayatilaka, M.A. Spackman, *CrystalExplorer*: a program for Hirshfeld surface analysis, visualization and quantitative analysis of molecular crystals, J. Appl. Crystallogr. 54 (3) (2021) 1006–1011, https://doi.org/10.1107/ S1600576721002910
- [45] C.F. Mackenzie, P.R. Spackman, D. Jayatilaka, M.A. Spackman, CrystalExplorer model energies and energy frameworks: extension to metal coordination compounds, organic salts, solvates and open-shell systems, IUCrJ 4 (5) (2017) 575–587, https://doi.org/10.1107/S205225251700848X.
- [46] M. Frisch, G. Trucks, H. Schlegel, G. Scuseria, M. Robb, J. Cheeseman, G. Scalmani, V. Barone, G. Petersson, H. Nakatsuji, Gaussian–16 Revision C. 01, 2019, Gaussian Inc., Wallingford CT Search PubMed.
- [47] M. Mehri, N. Chafai, L. Ouksel, K. Benbouguerra, A. Hellal, S. Chafaa, Synthesis, electrochemical and classical evaluation of the antioxidant activity of three α-aminophosphonic acids: experimental and theoretical investigation, J. Mol. Struct. 1171 (2018) 179–189, https://doi.org/10.1016/j.molstruc.2018.05.074.
- [48] R. Dennington, T.A. Keith, J.M. Millam, GaussView 6.0. 16, Semichem Inc.: Shawnee Mission, KS, USA (2016).
- [49] O. Trott, A.J. Olson, AutoDock Vina: improving the speed and accuracy of docking with a new scoring function, efficient optimization, and multithreading, J. Comput. Chem. 31 (2) (2010) 455–461, https://doi.org/10.1002/jcc.21334.
- [50] M.K. Gilson, H.-X. Zhou, Calculation of protein-ligand binding affinities, Annu. Rev. Biophys. Biomol. Struct. 36 (1) (2007) 21–42, https://doi.org/10.1146/annurev.biophys.36.040306.132550.